Armored MOFs: Enforcing Soft Microporous MOF Nanocrystals with Hard Mesoporous Silica

Zheng Li[†] and Hua Chun Zeng*[†,‡]

[†]NUS Graduate School for Integrative Sciences and Engineering, and Department of Chemical and Biomolecular Engineering, Faculty of Engineering, National University of Singapore, 10 Kent Ridge Crescent, Singapore 119260

[‡]Institute of Materials Research and Engineering (IMRE), 3 Research Link, Singapore 117602

S *Supporting Information*

ABSTRACT: Metal−organic frameworks (MOFs) are a class of fascinating supramolecular soft matters but with relatively weak mechanical strength. To enforce MOF materials for practical applications, one possible way seems to be transforming them into harder composites with a stronger secondary phase. Apparently, such a reinforcing phase must possess larger porosity for ionic or molecular species to travel into or out of MOFs without altering their pristine physicochemical properties. Herein we report a general synthetic approach to coat microporous MOFs and their derivatives with an enforcing shell of mesoporous silica ($mSiO_2$). Four well-known MOFs (ZIF-8, ZIF-7, UiO-66, and HKUST-1), representing two important families of MOFs, have served as a core phase in nanocomposite products. We show that significant enhancement in mechanical properties (hardness and toughness) can indeed be achieved with this "armoring approach". Excellent accessibility of the $mSiO_2$-wrapped MOFs and their metal-containing nanocomposites has also been demonstrated with catalytic reduction of 4-nitrophenol.
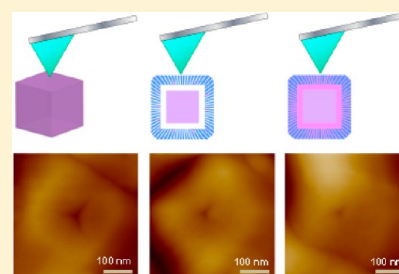
INTRODUCTION

Over the past decades, extensive research effort in metal−organic frameworks (MOFs) has given birth to thousands of MOFs.[1−4] As a class of supramolecular solids formed by bridging metal ions with organic linkers, the most outstanding properties of MOFs are assigned to their ultrahigh surface area and tunable composition and porosity, which have led to many potential applications in many existing and emerging technological fields.[5−7] In recent years, moreover, nanotechnology and nanoscience also add new functionalities to MOFs. For instance, size- and shape-controlled MOFs and their derived nanocomposites have opened up a new avenue for future applications.[8−11]

Despite all these advancements, low thermal stability and mechanical strength have been the two major drawbacks that limit the actual applications of this class of soft matters;[1,12,13] the maximum temperature that MOFs could sustain is reported only around 550 °C.[14] Compared to the metal−oxygen (M−O) bond, the metal−nitrogen (M−N) bond is usually much stronger. Therefore, thermally more stable MOFs could be attained with coordination bonding of M−N.[15] Furthermore, high moisture sensitivity is another common hurdle that turns away many MOFs from their practical application.[16] To circumvent this problem, developments of nitrogen-bearing MOFs or MOFs containing metals with higher coordination numbers, together with the postsynthetic modifications of organic linkers, have been made.[15,17−20] The mechanical properties of MOFs have also been investigated, which was focused on MOFs thin films or the microsized MOFs. For example, elastic modulus and hardness of some MOFs have been measured through a nanoindentation technique.[21−23] It should be pointed out that nonporous SiO_2 coating on the exterior surface of MOFs has been reported before to improve the MOFs stability for biomedical imaging.[24−26] Nevertheless, such SiO_2-coated MOFs cannot preserve the pristine microporosity of MOFs due to total pore blockage by the compact shell. Despite the efforts to find new MOFs with higher stabilities,[27,28] how to improve their mechanical properties, especially when working under harsh environments, remains as a crucial bottleneck for their practical usages.

Herein we report a general method to enhance the mechanical properties (i.e., relative hardness and toughness) of MOF materials and nanocomposites through solution-based chemical processes. In analogy to the armor on a tank, a harder mesoporous silica ($mSiO_2$) shell has been successfully deposited onto MOFs and nanocomposites as a reinforcing phase. Using atomic force microscopy (AFM) nanoindentation technique, we show that significant enhancement in mechanical properties can indeed be achieved for MOFs with this "armoring approach". Because the $mSiO_2$ has a larger pore size than MOFs, chemical reactants or adsorbates can easily penetrate through this shell and reach the core phases without deteriorating the intrinsic properties of MOFs.

EXPERIMENTAL SECTION

Materials. The following chemicals were used as received without further purification: $Zn(NO_3)_2 \cdot 6H_2O$ (98%, Sigma−Aldrich), 2-

methylimidazole (2-MeIM, 99%, Aldrich), benzimidazole (98%, Aldrich), Cu(NO$_3$)$_2$·3H$_2$O (99.5%, Merck), trimesic acid (95%, Aldrich), terephthalic acid (98%, Aldrich), ZrCl$_4$ (≥98%, Merck), tetraethyl orthosilicate (TEOS, ≥99%, Aldrich), acetic acid (100%, Merck), sodium acetate (99%, Alfa Aesar), HAuCl$_4$·3H$_2$O (≥99.9%, Aldrich), 3-mercaptopropionic acid (MPA, 99%, Lancaster), tetrabuty-lammonium borohydride (R-NBH$_4$, 98%, Sigma–Aldrich), hexadecyl-trimethyl-ammonium bromide (CTAB, 98%, Aldrich), cetyltrimethyl-ammonium chloride solution (CTAC, 25 wt % in H$_2$O, Aldrich), polyvinylpyrrolidone (PVP K30, MW = 40000, Fluka), 4-nitrophenol (≥99.5%, Fluka), sodium borohydride (NaBH$_4$, 99.99%, Sigma–Aldrich), N,N-dimethylformamide (DMF, AR, Merck), dimethyl sulfoxide (DMSO, 99.5%, Sigma), methanol (AR, Merck), and triethanolamine (TEA, 99+%, Acros Organics). Deionized water was collected through the Elga Micromeg Purified Water system. The mica sheet (V-1 grade) used for the AFM nanoindentation test was bought from SPI Supplies.

ZIF-8, ZIF-8@Au, and ZIF-8@Cu. ZIF-8 cubic nanocrystals and ZIF-8@Au nanocomposites were synthesized according to a method described in our previous publication,[29] except that the preparation of ZIF-8@Au was scaled up by 10 times. Copper nanoparticles (CuNPs) were also anchored on the exterior surface of ZIF-8[29] to form ZIF-8@Cu, except Cu(NO$_3$)$_2$·3H$_2$O was used as a copper precursor. After the preparation and sample washing process, ZIF-8@Au and ZIF-8@Cu nanocomposites were centrifuged and dried under vacuum overnight. The solid samples and the obtained ZIF-8 nanocubes were then dispersed into 20.0 mL of methanol for TEM analysis and further use.

UiO-66, UiO-66@Au, and UiO-66@Cu. UiO-66 octahedral nanocrystals were prepared through an approach reported before with some modifications.[30] Briefly, 0.0093 g of ZrCl$_4$ was first dissolved into 16.0 mL of 3.0 M acetic acid solution in DMF under ultrasonication. Then 4.0 mL of 40 mM terephthalic acid solution in DMF was injected into the mixture with stirring for another 5 min. The final mixture was transferred to a 50 mL Teflon-lined stainless steel autoclave and heated in an electric oven at 120 °C for 36 h. The products were harvested through centrifuging and washing twice with 20.0 mL of methanol each time. Finally the products were dispersed in 20.0 mL of methanol for TEM analysis and further use. UiO-66@Au and UiO-66@Cu nanocomposites were prepared with the similar procedures used for the ZIF-8@Au and ZIF-8@Cu samples, except using UiO-66 octahedral nanocrystals as cores. Moreover, 1 h of ultrasonication was needed in mixing UiO-66 with Au(I)-MPA hybrid or with CuNPs in order to form the coordination bonds.

ZIF-7 and HKUST-1. ZIF-7 rhombic dodecahedral nanocrystals were prepared using the similar approach for the synthesis of ZIF-8 nanocubes.[29] Briefly, 9.6 mL of 0.070 M Zn(NO$_3$)$_2$·6H$_2$O solution in DMF was mixed with 0.10 g of CTAB under stirring condition for 5 min at room temperature. Then 9.6 mL of 0.43 M benzimidazole solution in DMF was added into the above mixture and stirred for another 5 min, which was then transferred to a 50 mL Teflon-lined stainless steel autoclave and heated in an electric oven at 120 °C for 6 h. The products were harvested by centrifuging and washing twice with 20.0 mL of methanol each time. They were then dispersed in 20.0 mL of methanol for TEM analysis and future use. In preparing HKUST-1 octahedral nanocrystals, 2.44 g of Cu(NO$_3$)$_2$·3H$_2$O and 0.58 g of trimesic acid in 5.0 g of DMSO was mixed under ultrasonication for 30 min, which was then kept in an electric oven at 65 °C overnight.[31] Later, 1.0 mL of the above solution was injected into 10.0 mL of methanol containing 0.10 g of PVP with vigorously stirring at 55 °C for 90 min. The products were harvested by centrifuging and washing twice with 10.0 mL of methanol each time, and finally dispersed in 10.0 mL of methanol for TEM analysis and further use.

ZIF-8@mSiO$_2$, UiO-66@mSiO$_2$, ZIF-7@mSiO$_2$, HKUST-1@mSiO$_2$, and ZIF-8@metal@mSiO$_2$. All the above MOF nanocrystals and MOFs@metal (ZIF-8@Au and ZIF-8@Cu) nanocomposites can be used as cores for mSiO$_2$ coating. Taking ZIF-8 nanocrystals, for example, 5.0 mL of the above ZIF-8 methanolic suspension was mixed with a solution containing 33.0 mL of H$_2$O, 21.0 mL of methanol, and 0.25 g of 2-MeIM. The mixture was then sonicated for 5 min, followed by injecting 0.55 mL of CTAC aqueous solution and stirring for 20 min.

Then 0.40 mL of TEOS was added into this mixture dropwise within 3 min. The resultant mixture was stirred for another 1 h. The final products were harvested by centrifuging and washing three times with 40.0 mL of methanol each time, and later dried under vacuum overnight. Ethanol can also be used as an alcohol for hydrolysis of TEOS; it plays an important role for the thickness control of mSiO$_2$ shell. In this case, the presynthesized ZIF-8 nanocrystals were first dried and calcined under N$_2$ at 100 °C for 4 h. Then 20.0−50.0 mg of the ZIF-8 nanocrystals were dispersed into a solution containing 33.0 mL of H$_2$O, 20.0 mL of ethanol, and 0.25 g of 2-MeIM. Other conditions were kept exactly as those described above for the methanol case, except the reaction time was extended to 2 h. To remove the soft template CTAC in the mSiO$_2$ channels, final dried products were calcined in a N$_2$ flow (50.0 mL min^{-1}) at 250 °C for 7 h. Similar procedures (using methanol as the alcohol) were adopted for the syntheses of UiO-66@mSiO$_2$, ZIF-7@mSiO$_2$, and HKUST-1@mSiO$_2$ nanocomposites. In the HKUST-1@mSiO$_2$ case, 0.25 g of 2-MeIM was replaced by 0.50 g of sodium acetate, and the reaction time was extended to 2−3 h. ZIF-8@Au@mSiO$_2$ and ZIF-8@Cu@mSiO$_2$ nanocomposites could also be prepared similarly with 20.0 mg of the ZIF-8@Au or ZIF-8@Cu (in methanol; 1 h). Before coating the mSiO$_2$ shell, the core-materials were calcined respectively under a N$_2$ gas-flow (50.0 mL min^{-1}) at 250 °C for 7 h in order to improve their stability.

ZIF-8@mSiO$_2$@ZIF-8. Ten mg of the above calcined ZIF-8@mSiO$_2$ sample was first dispersed in 10.0 mL of 0.548 M 2-MeIM aqueous solution under ultrasonication for 10 min, after which 6.0 mL of 0.0168 M Zn(NO$_3$)$_2$·6H$_2$O aqueous solution was injected into the above mixture with stirring for 10−45 min. The products were centrifuged and washed with 16.0 mL of deionized water, then centrifuged and washed with 16.0 mL of methanol twice. The products were dispersed in 10.0 mL of methanol for TEM analysis and further use. The sample obtained was denoted as ZIF-8@mSiO$_2$@ZIF-8, noting that different amounts of ZIF-8 could be added by varying reaction parameters in this regrowth (or overgrowth) process.

Accessibility of mSiO$_2$ Shells. Pore accessibility of the mSiO$_2$ shell on the MOF nanocrystals and related nanocomposites was examined through the catalytic reduction of 4-nitrophenol by NaBH$_4$ in aqueous phase using the MOFs@metal@mSiO$_2$ samples. These catalytic materials were calcined in N$_2$ flow at 250 °C for 7 h before use. Briefly, 0.47 mL of 1.3 M NaBH$_4$ was mixed with 3.08 mL of 0.125 mM 4-nitrophenol aqueous solution, and the solution immediately changed from colorless to bright yellow. Then 0.20 mL of ZIF-8@Au@mSiO$_2$ or ZIF-8@Cu@mSiO$_2$ suspension in water (0.40 mg mL^{-1}) was added into the reaction system under stirring for 5 s, and transferred into a quartz cell for UV−vis measurement. UV−vis absorption spectra were recorded in the range of 200−600 nm to monitor the reaction process.

Samples for the Measurement of Mechanical Properties. To investigate their mechanical properties, ZIF-8, ZIF-8@mSiO$_2$ (after calcination), and ZIF-8@mSiO$_2$@ZIF-8 nanocomposites were tested with AFM nanoindentation technique. Prior to the measurement, ZIF-8 nanocubes and ZIF-8@mSiO$_2$ were calcined under a N$_2$ stream (50 mL min^{-1}) at 250 °C for 7 h. In the sample preparation, 10.0 mg of ZIF-8 or ZIF-8@mSiO$_2$ powder was dispersed into 4.0 mL of methanol containing 0.05 g of PVP through ultrasonication for 10 min; the mixture was stirred vigorously for another 2 h, in order to get nonaggregated particles. The obtained product was centrifuged and washed three times each with 4.0 mL of methanol, and then dispersed in 4.0 mL of methanol. Finally, 0.10 mL of the above suspension was diluted in 4.0 mL of methanol under ultrasonication for 10 min. One or two drops of this suspension were placed onto the surface of a mica sheet; the sample was dried and kept inside a vacuum desiccator before the measurements. The ZIF-8@mSiO$_2$@ZIF-8 sample was prepared by mixing 4.0 mL of the above ZIF-8@mSiO$_2$@ZIF-8 methanolic suspension with 0.05 g of PVP while keeping other preparative procedures unchanged.

Materials Characterization. The crystallographic information of the prepared samples was established with powder X-ray diffraction (XRD, Bruker D8 Advance, Cu Kα radiation, λ = 1.5406 Å). Morphological investigation was carried out with field-emission scanning electron microscopy (FESEM, JEOL, model JSM-6700F)
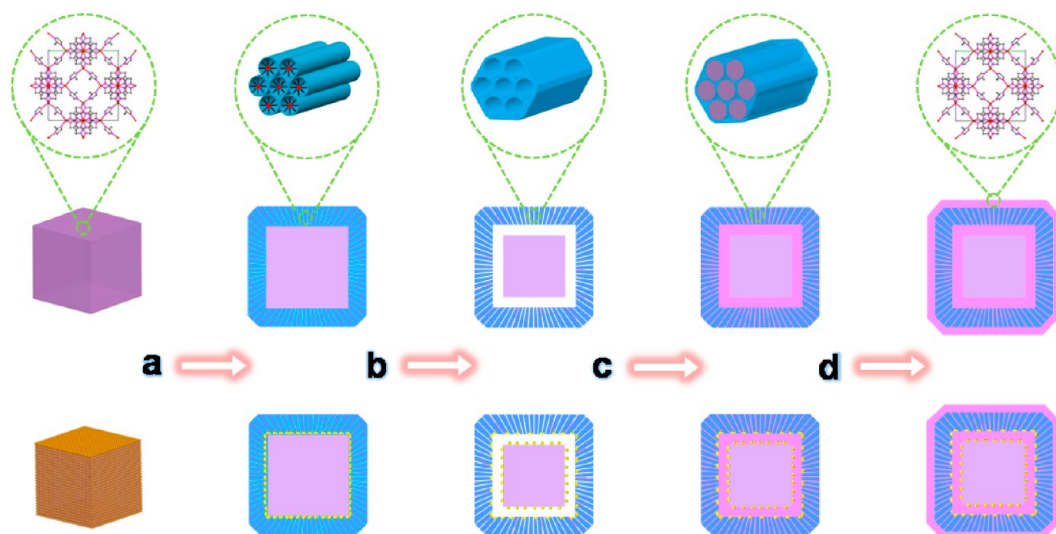
Figure 1. Preparations of mesoporous SiO_2 enforcing ZIF-8 and its nanocomposites: (a) deposition of gel-like SiO_2 shell on the ZIF-8 or ZIF-8@Au cores (the channels of SiO_2 shell are filled with CTAC molecules); (b) thermal conversion of gel-like SiO_2 to mesoporous SiO_2 (mSiO$_2$), together with partial infusion of ZIF-8 into the mSiO$_2$ shell; (c) regrowth of ZIF-8 to fill up the interior space of ZIF-8@mSiO$_2$ or ZIF-8@Au@mSiO$_2$; and (d) overgrowth of a new ZIF-8 shell on the surface of a mSiO$_2$ shell. The inserted graphics show the microporosity of ZIF-8 and the mesoporosity of mSiO$_2$. The purple color represents the ZIF-8 phase, and the blue color, the SiO_2 phase (light-blue lines indicate CTAC template in the mesopore channels of SiO_2), while the pink-purple color shows the refilled ZIF-8 phase after the regrowth or overgrowth process and the golden-yellow color represents the Au nanoparticles.
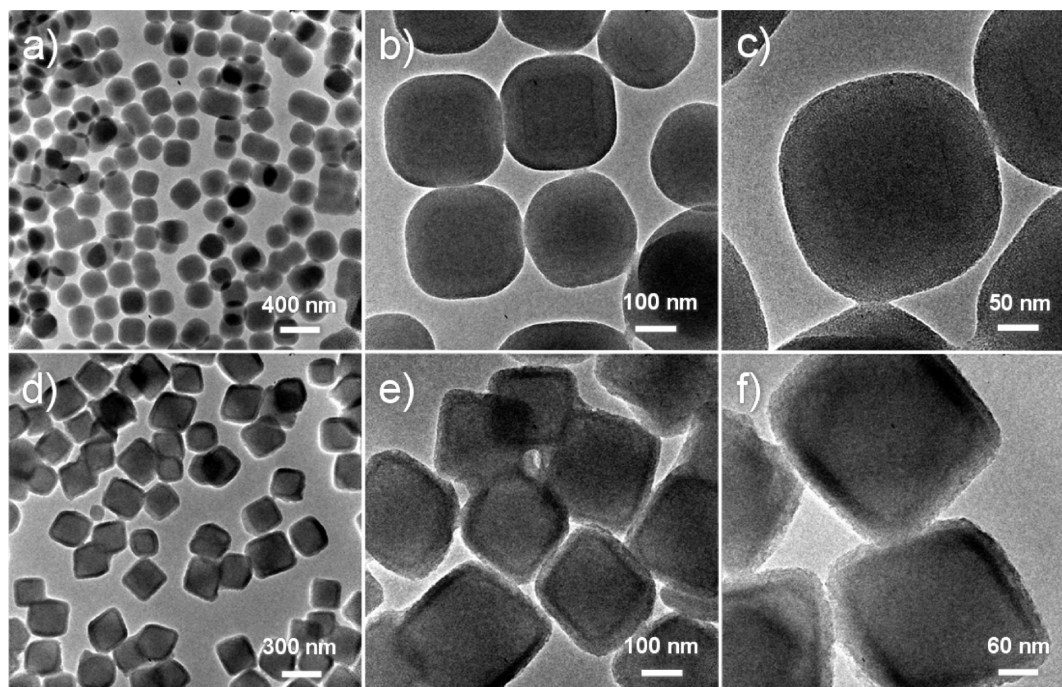

Figure 2. TEM images (a,b,c) at different magnifications for as-synthesized ZIF-8@mSiO$_2$ core−shell structures before calcination, with 5 mL of ZIF-8 (cubes) methanolic suspension as starting cores; and TEM images (d,e,f) at different magnifications for as-synthesized UiO-66@mSiO$_2$ core−shell structures before calcination, with 20 mL of UiO-66 (octahedrons) methanolic suspension as starting cores.

and transmission electron microscopy (TEM) (JEOL, model JEM-2010, 200 kV). Elemental line-scanning and mapping were conducted with EDX microanalysis (EDX/JEM-2100F, 200 kV). Specific surface areas of tested samples were determined using N_2 adsorption−desorption isotherms at 77 K (Quantachrome NOVA-3000 system) with the Brunauer−Emmett−Teller (BET) method, and the porosity was determined by NLDFT equilibrium method using the data of the desorption branch of isotherms. Prior to the measurement, samples were calcined at 250 °C under a N_2 flow for 7 h. Nanoindentation tests and atomic force microscopy (AFM; Bruker Dimension Icon) imaging

were performed using a diamond tip (PDNISP); the deflection sensitivity of the cantilever was 221 nm V^{-1} with the spring constant at 227 N m^{-1}.

■ RESULTS AND DISCUSSION

Figure 1 depicts two major synthetic routes developed in this work to prepare enforcing mSiO$_2$ shell coating on MOFs and nanocomposites (i.e., MOF@mSiO$_2$ and MOF@metal@mSiO$_2$). On the other hand, the resultant mSiO$_2$ shells can also
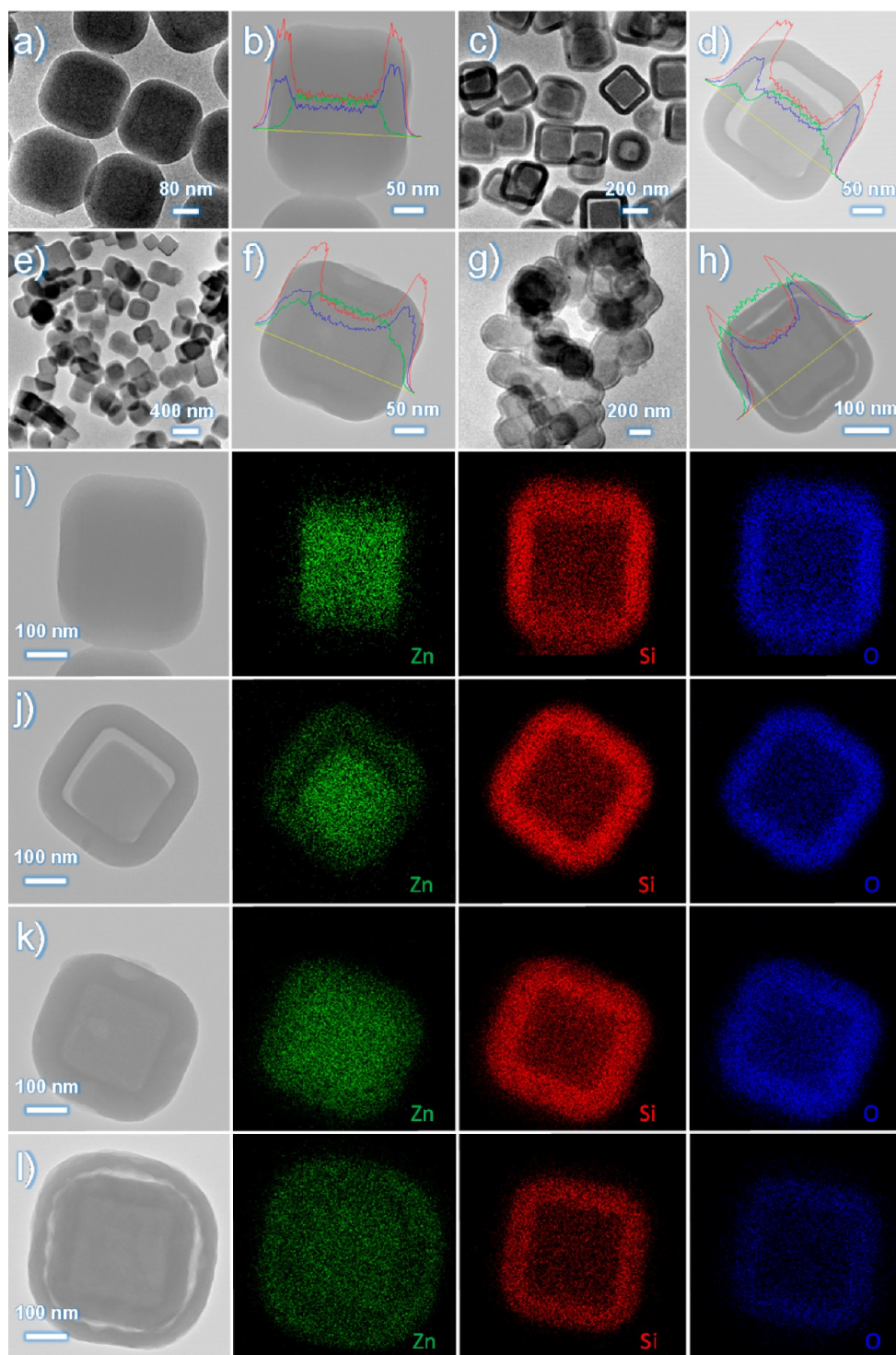
Figure 3. TEM images, line scans and corresponding elemental mappings of as-synthesized ZIF-8@*m*SiO$_2$ (a,b,l; before calcination); ZIF-8@*m*SiO$_2$ (c,d,j; after calcination); ZIF-8@*m*SiO$_2$@ZIF-8 (e,f,k; after regrowth); and ZIF-8@*m*SiO$_2$@ZIF-8 with another thick ZIF-8 shell (g,h,l; after overgrowth).

be coated with additional MOF phase(s), resulting in even more complex architectures MOF@*m*SiO$_2$@MOF and MOF@metal@*m*SiO$_2$@MOF. In Figure 2, two such core−shell nanostructures (with ZIF-8 and UiO-66 cores) are displayed. The generality of this approach is established by different types of MOFs (e.g., ZIF-8, ZIF-7, HKUST-1, and UiO-66) and crystal morphologies (e.g., cube, rhombic dodecahedron, and octahedron; Figure S1A in Supporting Information [SI]). The

structural characterization of the studied MOF materials can be referred to in Figure S1B−E in SI. It should be pointed out that the four selected samples in fact represent two important categories of coordinate bonds, N−M−N and −COO−M−OOC−, that constitute almost all the known MOFs.[1−4] Despite different coordination types and morphologies, all the MOF nanocrystals could be coated with SiO$_2$ shells (Figure 2 and Figure S2A−C in SI). The hybrid nanostructures show uniform
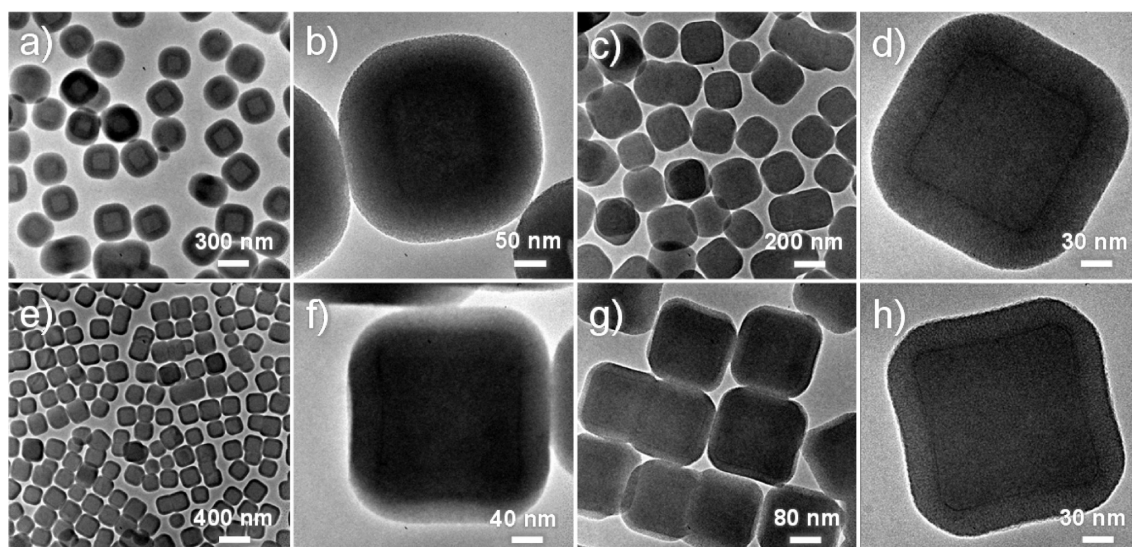
Figure 4. TEM images of ZIF-8@mSiO$_2$ with the different thicknesses for the mSiO$_2$ shell: (a,b) ZIF-8@mSiO$_2$−20, with the thickness ∼75 nm; (c,d) ZIF-8@mSiO$_2$−30, with the thickness ∼46 nm; (e,f) ZIF-8@mSiO$_2$−40, with the thickness ∼36 nm; and (g,h) ZIF-8@mSiO$_2$−50 with the thickness ∼26 nm. The numbers (20, 30, 40 and 50) denote the weight (mg) of ZIF-8 nanocubes used in synthesis.

thickness of the SiO$_2$ shell, with ∼60 nm for ZIF-8@SiO$_2$ and ∼30 nm for UiO-66@SiO$_2$ respectively (Figure 2). The MOF phases were well preserved with the mSiO$_2$ coating, while the overall morphologies of the products depend on the initial shape of the crystals. Subsequently, calcination of the as-synthesized ZIF-8@SiO$_2$ was carried out to remove the soft template cetyltrimethyl-ammonium chloride (CTAC) in the SiO$_2$ channels and to convert the gel-like SiO$_2$ shell to thermally stabilized mesoporous silica (mSiO$_2$; Figure S2A−C in SI).[32] To avoid possible oxidative decomposition of ZIF-8, this heat-treatment was held within a N$_2$ stream. The products show no phase evolution and color change (X-ray diffraction (XRD); Figure S3A and B in SI), noting that the hardened mSiO$_2$ shell is still amorphous. Nevertheless, infusion of ZIF-8 into the mSiO$_2$ shell was induced thermally, as revealed in Figure 3a−d and i−j. The gap generated between the mSiO$_2$ shell and MOF core can be filled up through the regrowth of ZIF-8 (Figure 3e−h). In this process, both Zn^{2+} ions and 2-MeIM linkers needed to diffuse through the mSiO$_2$ channels and deposit on the ZIF-8 cores. Special attention should be paid to the initial concentration of reactants, as a high concentration would also initiate spontaneous nucleation of ZIF-8 outside the core−shell nanostructures (Figure S3C in SI). After the regrowth, the mSiO$_2$ channels could also be filled up with ZIF-8. In Figure 3c−f and j−k, the intensity of Zn ions within the mSiO$_2$ shell has increased compared to that in the core phase (Figure S3D and E in SI; the mSiO$_2$ shell coating enhances overall mechanical strength of the products;[33] Figure 6). Also interestingly, if the regrowth proceeded for a longer time, e.g., 45 min, a three-layered architecture could be generated (ZIF-8@mSiO$_2$@ZIF-8; Figure 3g and Figure 1). The line scan profiles in Figure 3h and the elemental mappings in Figure 3l further confirm the composition of this outermost shell, noting that the XRD pattern also exhibits the phase pure ZIF-8 (Figure S3A in SI). In addition, MOFs@ metal nanocomposites, where gold and copper nanoparticles (AuNPs or CuNPs) are dispersed on the exterior surfaces of MOFs, can also serve as cores for mSiO$_2$ shells (Figure 1 and Figure S4A−E in SI). In these cases, the ZIF-8@Au or ZIF-8@ Cu was first heated under the N$_2$ atmosphere. As expected, infusion of ZIF-8 into the mSiO$_2$ shell also took place after

calcination, accompanied by development of gap space, while AuNPs or CuNPs were confined within the nanostructures (Figure S4C−E in SI). Similarly, the regrowth of ZIF-8 could also be performed in order to fill up the gap space. It should be noted that not all the MOFs would shrink during the calcination, since the infusion was mainly observed in the case of heated ZIF-8@ mSiO$_2$ sample. For the UiO-66@mSiO$_2$ and ZIF-7@mSiO$_2$, however, no obvious interior spaces were left after the same heat-treatment (Figure S2A and B in SI).

In order to preserve MOF cores while maintaining the alkaline environment required for hydrolyzing tetraethyl orthosilicate (TEOS), a rationale for the selection of the alkaline sources is essential. Taking ZIF-8, for example, we selected 2-methyl-imidazole (2-MeIM) for our synthesis because it is also the organic linker of a ZIF-8 framework. The pH value for the water−alcohol cosolvent solution with 0.25 g of 2-MeIM can reach up to 10.20, which is sufficient for the hydrolysis of TEOS. Besides ZIF-8, we have found that 2-MeIM also works well for the mSiO$_2$ coating on ZIF-7 and even on the UiO-66 which is a typical COO-based MOF (Figure S1A in SI). Nevertheless, it is not suitable for the mSiO$_2$ coating on HKUST-1 (Figure S1A in SI). In this latter case, sodium acetate was chosen by considering its weak basic property; the final pH value could reach up to 8.57 with 0.50 g of sodium acetate in synthesis (Experimental Section; longer reaction time was required). By choosing appropriate alkaline sources, the mSiO$_2$ phase and thus MOFs@mSiO$_2$ core− shell nanostructures can be prepared.

The hydrolysis rate of TOES can be further controlled by the composition of the water−alcohol cosolvent. With an increase of the carbon chain length of alkyl groups in alcohols, from methanol to n-butanol, the rate of TEOS hydrolysis would decrease, resulting in larger silica particles owing to a lower nucleation rate.[34] The fastest hydrolysis in the presence of methanol has been attributed to the high polarity, high hydrogen-bonding ability, and low viscosity of this alcohol.[35] It has been proposed and observed that there is an exchange process of alkoxy groups between the TEOS molecules and its surrounding alcohols, producing some intermediate derivatives that have different hydrolysis and condensation rates.[36] Compared to long-chain alcohols, methanol shows the least steric hindrance for the
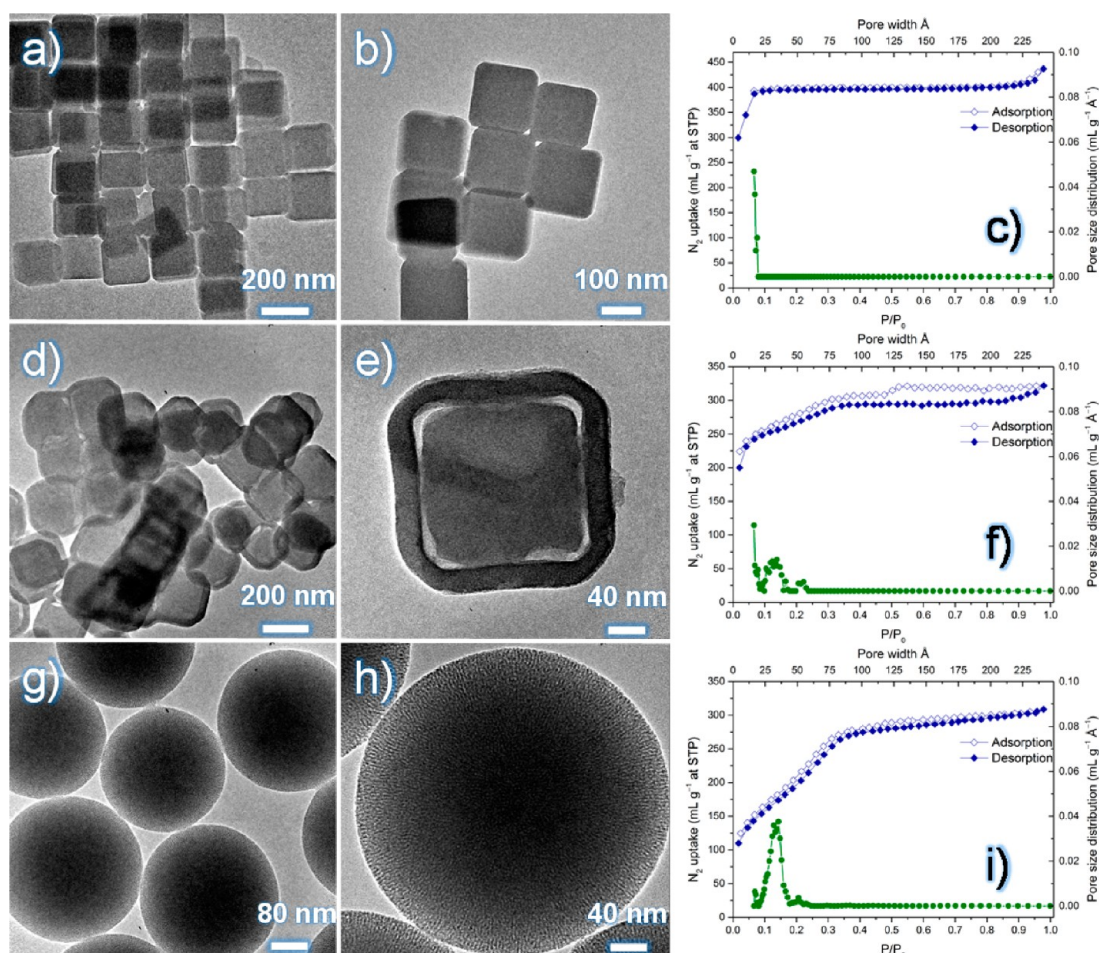
Figure 5. TEM images and textural investigations for pure ZIF-8 cubes (a,b,c), ZIF-8@mSiO$_2$ (d,e,f; after calcination), and pure mSiO$_2$ spheres (g,h,i).

exchange of alkoxy groups and thus the fastest nucleation of SiO$_2$. With the presence of methanol, the coating process could be completed within 1 h, whereas no obvious SiO$_2$ deposition was found with ethanol for the same period of time (Figure S5A in SI). If a longer reaction time with methanol was adopted, e.g., 2 h, freestanding SiO$_2$ particles would also be generated through homogeneous nucleation (Figure S5B in SI). For the silica coating on HKUST-1 cores, however, a longer reaction time was required, owing to the weaker alkaline environment adopted. The result of shell engineering is presented in Figure 4. In general, the thickness of mSiO$_2$ coating can be adjusted simply by varying the weight of ZIF-8 cores while the amount of TEOS is fixed. In this work, 20, 30, 40, and 50 mg of dried ZIF-8 were adopted, respectively, as cores for the shell coating. The ZIF-8 cores were first calcined under the N$_2$ flow at 100 °C for 4 h to remove the solvents and moistures trapped inside the ZIF-8. The coating reaction was conducted in the water−ethanol cosolvent (2 h; Experimental Section), and the thickness of the mSiO$_2$ shell can be tuned in the range of ∼26 to ∼75 nm upon the decrease of ZIF-8 cores from 50 to 20 mg.

With the mSiO$_2$ capping, the overall pore structure of the product can be tailor-made. For the pure ZIF-8, a type I adsorption−desorption isotherm was observed, and the steep increase for the N$_2$ uptake at low relative pressure reveals the microporosity of ZIF-8,[37] as shown in Figure 5a−c, noting that ZIF-8 has a pore diameter at 11.6 Å. The pure mSiO$_2$ shows the type IV isotherm with a faded H4 hysteresis loop, indicating the presence of mesopores with a uniform diameter at around 35 Å

(Figure 5i).[38] However, a mixed isotherm can be observed for the ZIF-8@mSiO$_2$ sample (Figure 5f), in which mesoporous mSiO$_2$ and microporous ZIF-8 are both effective for the N$_2$ adsorption− desorption, and therefore the isotherm should be assigned as a nonclassical type IV curve. The relative weak steep increase for the N$_2$ uptake at low relative pressure (below 0.1) reveals the microporosity contributed by the ZIF-8 phase, while the hysteresis loop confirms the mesoporous property of the mSiO$_2$ shell. It is noted that the hysteresis loop for the ZIF-8@ mSiO$_2$ is even more obvious than the pure mSiO$_2$, and the phenomenon should be attributed to the presence of large interior space after the calcination process (Figure 5e). For the ZIF-8@mSiO$_2$, the pore diameter at 35 Å is also present (Figure 5f), confirming the mesoporous silica shells. The specific BET surface areas decreased slightly after the coating of mSiO$_2$, and the measured values are 1500, 1000, and 780 m^2 g^{-1} for the pure ZIF-8, ZIF-8@mSiO$_2$, and pure mSiO$_2$ samples, respectively.

In this work, mechanical properties of MOFs and mSiO$_2$- coated MOFs nanomaterials were investigated for the first time using the AFM nanoindentation technique. Several approaches were employed to determine the relative hardness for the pure ZIF-8, ZIF-8@mSiO$_2$ (after calcination) and ZIF-8@mSiO$_2$@ ZIF-8 (Figure S6A in SI). The first method was the direct comparison of different projected areas (Figure S6B in SI). Under an identical indentation force, the size of projected areas could be used to compare the relative hardness of different materials. At a constant force of 8.02 μN, for example, the size of projected areas in Figure 6 shows this trend: ZIF-8 > ZIF-8@
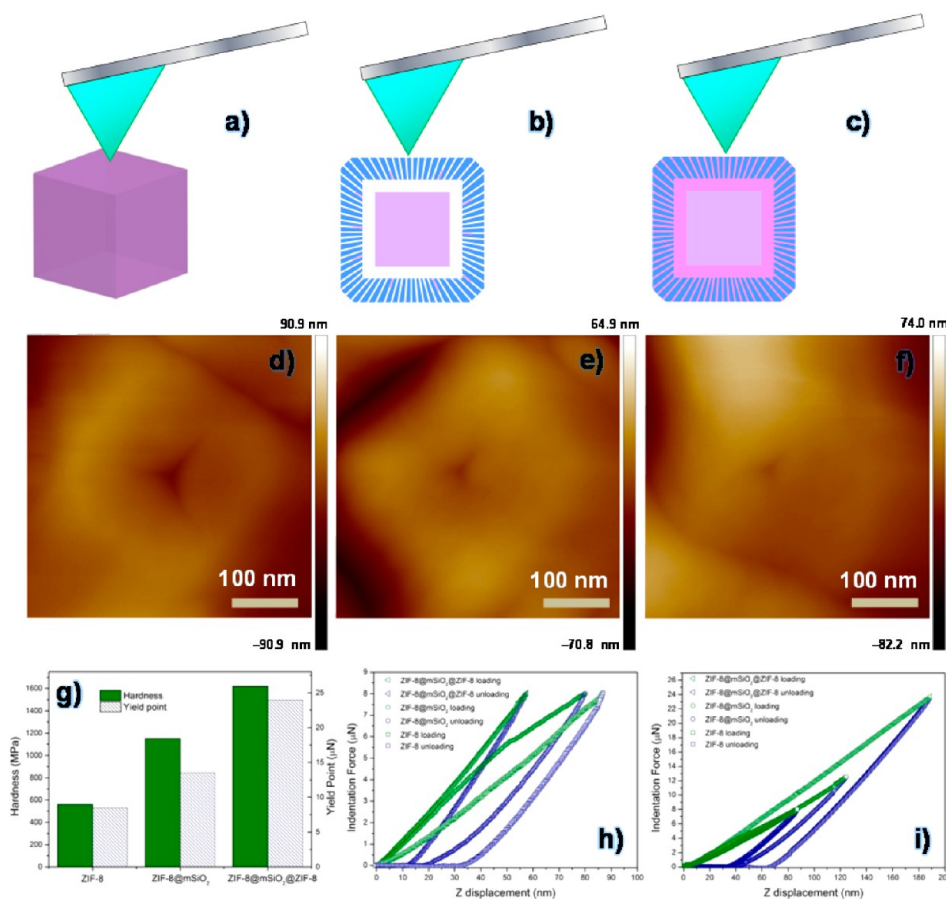
Figure 6. Model illustrations for the AFM nanoindentation on different nanostructures: (a) ZIF-8 cubes, (b) ZIF-8@mSiO$_2$ (after calcination), and (c) ZIF-8@mSiO$_2$@ZIF-8; AFM images after the indentation process, showing the triangle notch for (d) ZIF-8 cubes, (e) ZIF-8@mSiO$_2$ (after calcination), and (f) ZIF-8@mSiO$_2$@ZIF-8; (g) the calculated hardness and yield points for the above three nanostructures; (h) the force—displacement curves for the three nanostructures under the same indentation force at 8.02 μN; and (i) the force—displacement curves for the three nanostructures before the related yield points.

mSiO$_2$ > ZIF-8@mSiO$_2$@ZIF-8, and the hardness of the samples has a reverse sequence: ZIF-8@mSiO$_2$@ZIF-8 > ZIF-8@mSiO$_2$ > ZIF-8. The average projected areas can also be used to calculate the relative hardness under a constant indentation force with equation $H_A = F/A$, where H_A is the hardness, F represents the indentation force, and A is the projected area (Table S1 and Figure S6C in SI).[39−41] The average calculated results are shown in Figure 6g with an identical indentation force (8.02 μN). The calculated hardnesses for the pure ZIF-8, ZIF-8@mSiO$_2$, and ZIF-8@mSiO$_2$@ZIF-8 are 560, 1150, and 1620 MPa, respectively. To the best of our knowledge, this is the first time results to determine the relative hardness for a single piece of MOFs and their hybrid nanostructures, obtained using the nanoindentation technique. More importantly, it is the first example to enhance the mechanical strength of MOFs by introducing a reinforcing shell but without altering the intrinsic properties.

The improvement of hardness has been further verified from force—displacement curves (Figure 6h); several conclusions could be drawn. First, a larger slope of the force loading curve corresponds to the higher resistance of a tested material to indenting force, which in turn can be associated to the higher relative hardness of the material. Second, the total penetration depth (i.e., Z-displacement) is observed to decrease from the pure ZIF-8 to ZIF-8@mSiO$_2$ (after calcination), and finally to ZIF-8@mSiO$_2$@ZIF-8. In Figure 6h, the maximum Z-displacement for the pure ZIF-8 at 8.02 μN can reach up to 87 nm, while

the values for the ZIF-8@mSiO$_2$ (after calcination) and ZIF-8@mSiO$_2$@ZIF-8 are 80 and 57 nm, respectively. These results reflect different resistances to the same indenting force, and thus the relative hardness can be derived. And third, the maximum Z-displacement contains both elastic and plastic deformation regions, where the elastic part can be defined by the force unloading region of the curve with a steep slope, and the plastic part can be identified from the intersection point between the unloading curve and X-axis (where F is switched to zero). Figure 6h indicates that the final depth of the triangle notch left over on the pure ZIF-8, ZIF-8@mSiO$_2$, and ZIF-8@mSiO$_2$@ZIF-8 is 32, 18, and 10 nm, respectively, which could also serve as a judgment of hardness. Quite interestingly, variation in the force loading slope is often observed for the ZIF-8@mSiO$_2$ (after calcination; Figure 6h). This observation should be attributed to the existence of the gap space between the core and shell. In this indentation process, the ZIF-8 core might slide slightly inside the mSiO$_2$ shell, because of the presence of the empty space (Figures 2c−d).

The yield point of each material is another measurement to account for the hardness and toughness. Here it is defined as the maximum force applied to a tested material without causing breakage or crush, and it can be determined directly from both AFM topographical image and force—displacement curve. In such a test, a crack on particles can be observed if the indentation force reaches the yield point (Figure S6D in SI). A fluctuating
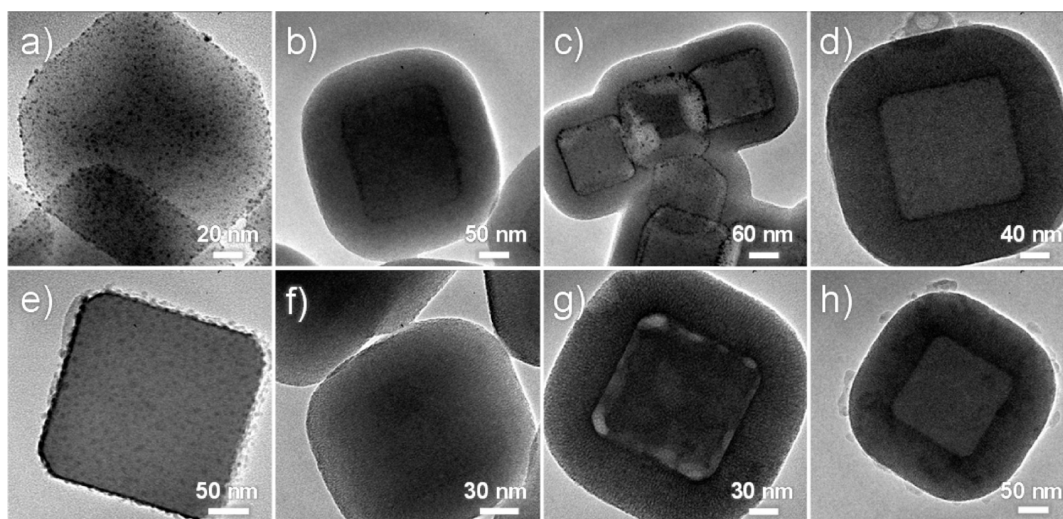
Figure 7. TEM images for (a) ZIF-8@Au after calcination, (b) ZIF-8@Au@mSiO$_2$ before calcination, (c) ZIF-8@Au@mSiO$_2$ after calcination, (d) ZIF-8@Au@mSiO$_2$@ZIF-8, (e) ZIF-8@Cu after calcination, (f) ZIF-8@Cu@mSiO$_2$ before calcination, (g) ZIF-8@Cu@mSiO$_2$ after calcination, (h) ZIF-8@Cu@mSiO$_2$@ZIF-8.
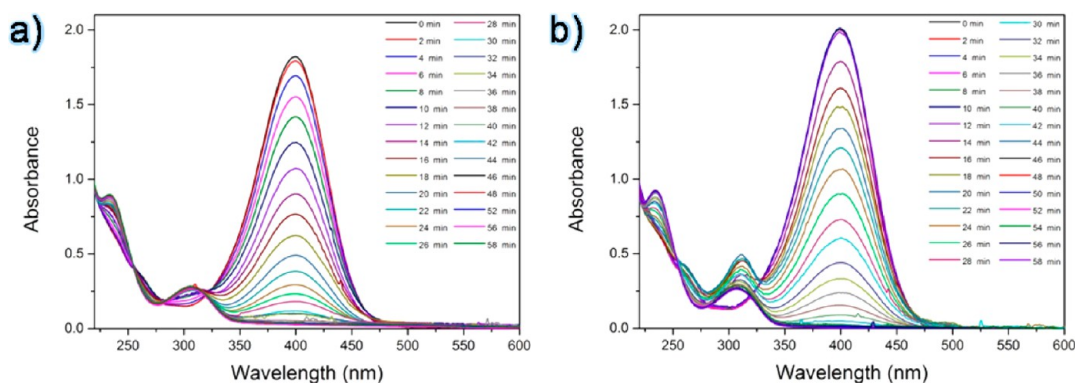

Figure 8. Accessibility of mSiO$_2$ shell in catalytic reaction: sequential UV−vis spectra during the reduction reaction of 4-nitrophenol using catalysts of (a) ZIF-8@Au@mSiO$_2$ and (b) ZIF-8@Cu@mSiO$_2$.

point can also be found in the loading curve in response to the breakage or crush. In this work, the measured yield points are 8.5, 13.5, and 24 μN (Figure 6i) for ZIF-8, ZIF-8@mSiO$_2$ (after calcination), and ZIF-8@mSiO$_2$@ZIF-8, respectively. At the same time, relative toughness can also be compared among the samples, which is defined by the maximum plastic deformation before crushing. As anticipated in Figure 6i, maximum elastic and plastic deformations have increased significantly for ZIF-8@mSiO$_2$@ZIF-8, compared to the unprotected ZIF-8. Enhanced toughness can also be confirmed with the force−displacement curves for the ZIF-8@mSiO$_2$@ZIF-8, which can be referred to in Figure S6E in SI. Therefore, we name this new type of hybrid materials as the "armored MOFs".

Compared with the soft MOF materials, mesoporous silica is more rigid because of the strong Si−O bond. Therefore the MOF nanostructures with the mesoporous silica shell should show a better mechanical performance compared with the pure MOF nanostructures. Accordingly, among the above three structures in Figure 6, the pure ZIF-8 nanoparticles show the worst mechanical property. The different mechanical properties between ZIF-8@mSiO$_2$ and ZIF-8@mSiO$_2$@ZIF-8 can be attributed to their different structural/compositional features. For example, the gap space, which was generated after heating, between the ZIF-8 core and mSiO$_2$ shell led to less mechanical

enhancement for the overall product. Nevertheless, the mesoporous silica is in close contact with ZIF-8 phase in the ZIF-8@mSiO$_2$@ZIF-8 (Figure 3e,f,k), and the shells supported with the solid interior should exhibit a better mechanical performance compared with those without any support (i.e., the gap space). Moreover, enhanced mechanical strengths can be attained by forming hybrid materials.[33] In the above case, the mesoporous silica shell together with ZIF-8 in its channels should also be considered as a hybrid material. As a result, the ZIF-8@mSiO$_2$@ZIF-8 should show the best mechanical properties among the three products investigated in Figure 6.

Apart from the low temperature physisorption condition (Figure 5), accessibility of armored MOFs has also been tested under real reaction environments. In particular, ZIF-8@Au and ZIF-8@Cu nanocomposites (Figure S4C−E in SI) were chosen as catalysts for this test. It was found that CuNPs are not stable in air, especially with the presence of moistures (oxidative color change from yellow Cu^0 to green Cu$^+$; Figure S4E in SI). After calcination in N$_2$, surface species Cu$_2$S (XPS; Figure S4E in SI) was found. As shown in Figure 7, ZIF-8@Au and ZIF-8@Cu were used as binary solid cores for the mSiO$_2$ coating. The resultant ZIF-8@Au@mSiO$_2$ and ZIF-8@Cu@mSiO$_2$ were examined respectively for their catalytic activity using reduction of 4-nitrophenol as a model reaction. In Figure 8, the two

catalysts both show good performance over the reduction of 4-nitrophenol by NaBH$_4$. Nevertheless, a longer induction time was observed for the ZIF-8@Cu@mSiO$_2$ nanocomposites in this reaction, since an additional reduction of surface Cu$_2$S to Cu^0 at the beginning was required before the catalytic reduction of 4-nitrophenol by NaBH$_4$. This reaction confirms that the enforcing mSiO$_2$ shells are indeed permeable for the reactant and product chemicals involved in this reaction.

CONCLUSIONS

In summary, we have developed a general approach to prepare the "armored MOFs" core–shell nanocomposites with controllable mSiO$_2$ shells as a reinforcing phase, which plays an important role in preserving the microporosity and other pristine physicochemical properties of MOF cores. With the assistance of the mSiO$_2$ shells, at the same time, the mechanical properties (the relative hardness and toughness) of the MOFs have been improved significantly. The mSiO$_2$ armored MOFs can be further functionalized with additional material phases. Excellent accessibility of ionic or molecular species traveling into or out of the MOF phase has been demonstrated with the reduction reaction of 4-nitrophenol by NaBH$_4$ in aqueous solution. We believe that our approach could open up a new research direction for making practical multifunctional MOF materials.

ASSOCIATED CONTENT

S **Supporting Information**

Additional SEM and TEM images, illustrated crystal structures, XRD, XPS, elemental mappings, and AFM nanoindentation test results. This material is available free of charge via the Internet at http://pubs.acs.org.

AUTHOR INFORMATION

Corresponding Author

chezhc@nus.edu.sg

Notes

The authors declare no competing financial interest.

ACKNOWLEDGMENTS

REFERENCES

(1) Férey, G. *Chem. Soc. Rev.* **2008**, *37*, 191.

(2) James, S. L. *Chem. Soc. Rev.* **2003**, *32*, 276.

(3) Kitagawa, S.; Kitaura, R.; Noro, S.-I. *Angew. Chem., Int. Ed.* **2004**, *43*, 2334.

(4) Yaghi, O. M.; O'Keeffe, M.; Ockwig, N. W.; Chae, H. K.; Eddaoudi, M.; Kim, J. *Nature* **2003**, *423*, 705.

(5) Britt, D.; Tranchemontagne, D.; Yaghi, O. M. *Proc. Natl. Acad. Sci. U.S.A.* **2008**, *105*, 11623.

(6) Horcajada, P.; Chalati, T.; Serre, C.; Gillet, B.; Sebrie, C.; Baati, T.; Eubank, J. F.; Heurtaux, D.; Clayette, P.; Kreuz, C.; Chang, J.-S.; Hwang, Y. K.; Marsaud, V.; Bories, P.-N.; Cynober, L.; Gil, S.; Férey, G.; Couvreur, P.; Gref, R. *Nat. Mater.* **2010**, *9*, 172.

(7) Lee, J.; Farha, O. K.; Roberts, J.; Scheidt, K. A.; Nguyen, S. T.; Hupp, J. T. *Chem. Soc. Rev.* **2009**, *38*, 1450.

(8) Jiang, H. L.; Xu, Q. *Chem. Commun.* **2011**, *47*, 3351.

(9) Lin, W.; Rieter, W. J.; Taylor, K. M. L. *Angew. Chem., Int. Ed.* **2009**, *48*, 650.

(10) Lu, G.; Li, S.; Guo, Z.; Farha, O. K.; Hauser, B. G.; Qi, X.; Wang, Y.; Wang, X.; Han, S.; Liu, X.; DuChene, J. S.; Zhang, H.; Zhang, Q.; Chen, X.; Ma, J.; Loo, S. C. J.; Wei, W. D.; Yang, Y.; Hupp, J. T.; Huo, F. *Nat. Chem.* **2012**, *4*, 310.

(11) Spokoyny, A. M.; Kim, D.; Sumrein, A.; Mirkin, C. A. *Chem. Soc. Rev.* **2009**, *38*, 1218.

(12) Davis, M. E. *Nature* **2002**, *417*, 813.

(13) Ma, L.; Abney, C.; Lin, W. *Chem. Soc. Rev.* **2009**, *38*, 1248.

(14) Kang, I. J.; Khan, N. A.; Haque, E.; Jhung, S. H. *Chem.—Eur. J.* **2011**, *17*, 6437.

(15) Colombo, V.; Galli, S.; Choi, H. J.; Han, G. D.; Maspero, A.; Palmisano, G.; Masciocchi, N.; Long, J. R. *Chem. Sci.* **2011**, *2*, 1311.

(16) Kaye, S. S.; Dailly, A.; Yaghi, O. M.; Long, J. R. *J. Am. Chem. Soc.* **2007**, *129*, 14176.

(17) Liu, J.; Thallapally, P. K.; McGrail, B. P.; Brown, D. R.; Liu, J. *Chem. Soc. Rev.* **2012**, *41*, 2308.

(18) Cavka, J. H.; Jakobsen, S.; Olsbye, U.; Guillou, N.; Lamberti, C.; Bordiga, S.; Lillerud, K. P. *J. Am. Chem. Soc.* **2008**, *130*, 13850.

(19) Ma, D.; Li, Y.; Li, Z. *Chem. Commun.* **2011**, *47*, 7377.

(20) Joseph, G. N.; Seth, M. C. *J. Am. Chem. Soc.* **2010**, *132*, 4560.

(21) Tan, J. C.; Bennett, T. D.; Cheetham, A. K. *Proc. Natl. Acad. Sci. U.S.A.* **2010**, *107*, 9938.

(22) Tan, J. C.; Cheetham, A. K. *Chem. Soc. Rev.* **2011**, *40*, 1059.

(23) Bundschuh, S.; Kraft, O.; Arslan, H. K.; Gliemann, H.; Weidler, P. G.; Wöll, C. *Appl. Phys. Lett.* **2012**, *101*, 101910.

(24) Taylor, K. M. L.; Rieter, W. J.; Lin, W. *J. Am. Chem. Soc.* **2008**, *130*, 14358.

(25) Taylor-Pashow, K. M. L.; Rocca, J. D.; Xie, Z.; Tran, S.; Lin, W. *J. Am. Chem. Soc.* **2009**, *131*, 14261.

(26) Rieter, W. J.; Taylor, K. M. L.; Lin, W. *J. Am. Chem. Soc.* **2007**, *129*, 9852.

(27) Wu, H.; Yildirim, T.; Zhou, W. *J. Phys. Chem. Lett.* **2013**, *4*, 925.

(28) Guillerm, V.; Ragon, F.; Dan-Hardi, M.; Devic, T.; Vishnuvarthan, M.; Campo, B.; Vimont, A.; Clet, G.; Yang, Q.; Maurin, G.; Férey, G.; Vittadini, A.; Gross, S.; Serre, C. *Angew. Chem., Int. Ed.* **2012**, *51*, 9267.

(29) Li, Z.; Zeng, H. C. *Chem. Mater.* **2013**, *25*, 1761.

(30) Lu, G.; Cui, C.; Zhang, W.; Liu, Y.; Huo, F. *Chem.—Asian J.* **2013**, *8*, 69.

(31) Ameloot, R.; Gobechiya, E.; Uji-i, H.; Martens, J. A.; Hofkens, J.; Alaerts, L.; Sels, B. F.; De Vos, D. E. *Adv. Mater.* **2010**, *22*, 2685.

(32) Dou, J.; Zeng, H. C. *J. Am. Chem. Soc.* **2012**, *134*, 16235.

(33) Alexandre, M.; Dubois, P. *Mater. Sci. Eng., R* **2000**, *28*, 1.

(34) Stober, W.; Fink, A.; Bohn, E. *J. Colloid Interface Sci.* **1968**, *26*, 62.

(35) Brinker, C. J. *J. Non-Cryst. Solids* **1988**, *100*, 31.

(36) Lim, J.; Ha, S.-W.; Lee, J.-K. *Bull. Korean Chem. Soc.* **2012**, *33*, 1067.

(37) Park, K. S.; Ni, Z.; Cote, A. P.; Choi, J. Y.; Huang, R.; Uribe-Romo, F. J.; Chae, H. K.; O'Keeffe, M.; Yaghi, O. M. *Proc. Natl. Acad. Sci. U.S.A.* **2006**, *103*, 10186.

(38) Sing, K. S.; Everett, D. H.; Haul, R. A. W.; Moscou, L.; Pierotti, R. A.; Rouquerol, J.; Siemieniewska, T. *Pure Appl. Chem.* **1985**, *57*, 603.

(39) Bhushan, B.; Koinkar, V. N. *Appl. Phys. Lett.* **1994**, *64*, 1653.

(40) Calabri, L.; Pugno, N.; Menozzi, C.; Valeri, S. *J. Phys.: Condens. Matter* **2008**, *20*, 474208.

(41) Oliver, W. C.; Pharr, G. M. *J. Mater. Res.* **2004**, *19*, 3.